RESEARCH ARTICLE

Key Points:
- Bubble size distributions (0.5–60 μm radius) were measured during wave breaking
- Bubbles ≤ 30 μm in radius supplied $\sim 30\%$ of the void fraction at 4 m depth
- Bubble populations were presented in the context of wind and wave conditions

Correspondence to:
K. Randolph,
kaylan.randolph@uconn.edu

Optical measurements of small deeply penetrating bubble populations generated by breaking waves in the Southern Ocean

Kaylan Randolph[1], Heidi M. Dierssen[1], Michael Twardowski[2], Alejandro Cifuentes-Lorenzen[1], and Christopher J. Zappa[3]

[1]Department of Marine Sciences, University of Connecticut, Groton, Connecticut, USA, [2]WET Labs Inc., Narragansett, Rhode Island, USA, [3]Lamont-Doherty Earth Observatory of Columbia University, Palisades, New York, USA

Abstract Bubble size distributions ranging from 0.5 to 125 μm radius were measured optically during high winds of 13 m s^{-1} and large-scale wave breaking as part of the Southern Ocean Gas Exchange Experiment. Very small bubbles with radii less than 60 μm were measured at 6–9 m depth using optical measurements of the near-forward volume scattering function and critical scattering angle for bubbles ($\sim 80°$). The bubble size distributions generally followed a power law distribution with mean slope values ranging from 3.6 to 4.6. The steeper slopes measured here were consistent with what would be expected near the base of the bubble plume. Bubbles, likely stabilized with organic coatings, were present for time periods on the order of 10–100 s at depths of 6–9 m. Here, relatively young seas, with an inverse wave age of approximately 0.88 and shorter characteristic wave scales, produced lower bubble concentrations, shallower bubble penetration depths, and steep bubble size distribution slopes. Conversely, older seas, with an inverse wave age of 0.70 and longer characteristic wave scales, produced relatively higher bubble concentrations penetrating to 15 m depth, larger bubble sizes, and shallower bubble size distribution slopes. When extrapolated to 4 m depth using a previously published bubble size distribution, our estimates suggest that the deeply penetrating small bubbles measured in the Southern Ocean supplied $\sim 36\%$ of the total void fraction and likely contributed to the transfer and supersaturation of low-solubility gases.

1. Introduction

Bubble populations are recurrently introduced into the surface ocean by wind-generated, large-scale breaking waves. During high wind regimes, the transfer of lower-solubility gases (i.e., N_2 and O_2) is thought to become largely a bubble-mediated process [*Broecker and Siems*, 1984; *Woolf and Thorpe*, 1991; *Vagle et al.*, 2010]. Small, deeply penetrating bubbles dissolve even when the gas is saturated with respect to the atmosphere due to hydrostatic pressure and surface tension effects. As depth increases, the supersaturating effect of bubbles increases and the range of bubble sizes contributing to the gas flux narrows and shifts toward smaller sizes [*Woolf*, 1997; *Vagle et al.*, 2010]. The smallest bubbles collapse completely contributing 1–2 times more to the gas flux than the large bubbles that transfer only a fraction of their volume before rising out of the water column [*Hamme and Emerson*, 2006]. To date, bubble measurements, particularly in the smallest size ranges, are incomplete largely due to technological limitations [*Woolf et al.*, 2007].

Optical and acoustical techniques have been utilized for measuring oceanic bubble size distributions. Acoustical methods have been developed to sample the entire bubble cloud at high temporal and spatial resolution. The most commonly employed technique uses measurements of acoustical attenuation at multiple frequencies corresponding to the resonant frequencies of the bubbles present [*Medwin*, 1970; *Medwin and Breitz*, 1989; *Farmer et al.*, 1998; *Vagle and Farmer*, 1998]. Generally, resonant peaks over a frequency range of 5–400 kHz are used to capture bubble sizes from 20 to 500 μm in radius.

Past studies have used optical methods to resolve bubbles with radii as small as 10 μm [*Su et al.*, 1987; *O'Hern et al.*, 1988], but such methods sample only small volumes of water (generally mm^3 to cm^3) and cannot easily resolve the spatial and temporal variability inherent to bubble plumes. One of the most frequently cited bubble data sets was acquired using a photographic method [*Johnson and Cooke*, 1979]. More recently, *Deane and Stokes* [2002] used a video microscope to capture images of bubble plumes at time

periods on the order of milliseconds, but only bubbles larger than $\sim$80 μm in radius were measured. Consequently, the shape of the bubble size distribution in the small size classes is still in question.

Here new technology based on light scattering properties is used to identify bubbles in the water column and to estimate bubble size distributions during large-scale wave breaking (section 3.1). An air bubble in water has a relative refractive index of 0.75 and so bubbles produce a unique pattern of scattering. A bubble that is large relative to the wavelength of light will produce internal reflection within the water medium at approximately 82°, dubbed "the critical scattering angle." The scattering efficiency for bubbles at this angle is an order of magnitude greater than other oceanic particle types [*Zhang et al.*, 2002]. No other natural mechanism is known to augment scattering at this angle in oceanic waters. If air bubbles are present in the water column, enhanced scattering at the critical angle will be observed and can be measured using volume scattering sensors [*Zhang et al.*, 2002; *Twardowski et al.*, 2012]. In addition, optical methods based on laser diffraction are used to estimate the size distribution of oceanic particles, including bubbles [*Agrawal and Pottsmith*, 2000].

Bubble size distributions from 0.5 to 125 μm radius, measured optically at 6–9 m depths, are presented here. These bubbles were measured in open ocean conditions during the Southern Ocean Gas Exchange Experiment (SO GasEx) [*Ho et al.*, 2011]. A portion of the bubble size distribution extends toward smaller size classes than previously measured, however, where the size distribution overlaps with those previously reported, the shape and slope were compared for consistency (section 3.2). The evolution of each bubble event was traced through time using the high-frequency (1 Hz) measurements of bubble number concentration and size distribution slope (section 3.3).

Bubble size distributions and bubble plume characteristics are a direct result of the wind and wave conditions. Therefore, the bubble observations measured here were coupled with wind and wave statistics to aid in the interpretation of the bubble size distribution, slope and number concentration, bubble plume penetration depth, and void fraction (section 3.4). In order to assess the significance of small bubbles (<30 μm) to the total void fraction, an extrapolation of the bubble size distribution to 4 m was conducted (section 3.5). Finally, the potential bubble-mediated air-sea transfer of low-solubility gases (i.e., O_2) was considered within the context of dissolved gas measurements presented by *Moore et al.* [2011] and by extension of the *Woolf and Thorpe* [1991] wind-based oxygen supersaturation model to the smaller bubble sizes measured here (section 3.6).

2. Methodology

This investigation was conducted on the NOAA ship the *R.V. Ronald H. Brown* in the Atlantic sector of the Southern Ocean (50°S, 40°W), 7 March to 4 April 2008. The primary objective of SO GasEx was to measure gas transfer at high wind speeds (>10 m s^{-1}) and to identify predictors, in addition to wind, for estimating gas transfer [*Ho et al.*, 2011]. A Lagrangian approach was taken to study relevant chemical and biological processes. Two tracer patches were deployed lasting 6 and 15 days in duration, respectively. This study focuses on five total stations, including two stations sampled during high wind conditions and two control stations (sampled during low wind conditions) within Patch 2 and a single station sampled during high wind conditions 300 km north of South Georgia Island.

2.1. Optical Measurements

An optical package was deployed close to noon daily in the center of the patch area. Sensors on the package included a MASCOT volume scattering meter (WET Labs) and a LISST-100X diffractometer particle size analyzer (Sequoia Scientific, Inc.), positioned 15 cm apart. The optical package was suspended approximately 3 m from the starboard side of the ship using a winch. Measurements were collected as a 30 min time series. As a result of the strong wind and wave conditions, the package was deployed at deeper (>5 m) depths and oscillated vertically between 6 and 9 m. The close proximity of the package to the ship during deployment was not ideal and some contamination could have resulted. However, the location of the winch relative to the ship's thrusters (12–26 m distance) and the position of the ship while on-station, with the bow heading into the wind, helped to minimize these effects.

Bubble populations were determined using both the MASCOT measurements of the wide-angle volume scattering function and the LISST measurements of the particle size distribution. The presence of bubbles was identified based on enhancements in the volume scattering function at the critical angle. The

RANDOLPH ET AL. 2

measurement of particle size distribution, determined from the near-forward diffraction of light, distinguished particles primarily on size and not composition. Hence, the measured concentration of particles included all suspended particles, as well as bubbles. During high wind and wave events, simultaneous enhancements occurring in both the VSF at the critical angle and in the particle concentration measured using the LISST were indicative of bubbles (see below).

2.1.1. Measurements of Critical Angle Scattering

Bubbles were detected from enhancements in critical angle scattering, determined from measurements of the volume scattering function (VSF). The VSF, $\beta(\theta)$, describes the angular distribution of scattered light

$$\beta(\theta) = dI(\theta)/EdV \quad (\mathrm{m}^{-1}\mathrm{sr}^{-1}) \tag{1}$$

where I is the scattered intensity in the direction θ by the volume dV, with incident irradiance E. The VSF between 10° and 170° (in 10° increments) was measured at high frequency (20 Hz) using a MultiAngle SCattering Optical Tool (MASCOT, WET Labs). Details of the MASCOT design, calibration, and data processing are described in *Sullivan and Twardowski* [2009] and *Twardowski et al.* [2012].

The shape of the VSF augmentation at the critical angle, relative that that measured during low wind conditions, is indicative of the concentration of the bubbles present. Critical angle scattering observations containing bubbles were identified by comparing the distribution of the high wind observations to a single control, calculated as the mean of the measurements collected during low wind speeds and no wave breaking. The critical angle scattering data from each station were normalized by the sum of the data record to facilitate the direct comparison of distribution shapes. The appropriate statistical distribution was applied to the data using the Kolmogorov-Smirnof test ($\alpha = 0.05$) as the metric for determining the optimal fit. Statistical measures were calculated accordingly. Measurements of bubbles were identified as the portion of the probability density function of critical angle scattering measurements collected during high winds not intersecting with the distribution of the control.

2.1.2. Measurement of Bubble Size Distributions

Measurements of the particle size distribution (PSD), the size and number of all particles 0.5–125 μm in radius, including bubbles, were determined using the LISST-100X Type B (Laser In Situ Scattering and Transmissiometry, Sequoia Scientific, Inc.). The LISST measures laser diffraction, specifically the near-forward volume scattering function (0.07°–15° in water), at 32 logarithmically spaced silicon ring detectors. The volumetric particle concentration is nominally determined using the scattering intensity across the 32 detectors and an inverse transform based on Mie theory. The term "particle" here includes organic, inorganic, and air-filled (bubble) particles. The term "particulate" refers to all solid particles (i.e., inorganic and organic particles) and excludes bubbles. LISST data were processed following *Agrawal and Pottsmith* [2000] and *Andrews et al.* [2011]. Issues exist with the matrix inversion of the LISST raw scattering data, particularly at the large angles, which correspond to the smallest particle sizes. A "rising tail" in the particle size distribution can result when high concentrations of submicron particles are present. The raw scattering measurements were filtered using a three-point running average to smooth small irregularities caused by the presence of nonspherical particles [*Agrawal and Traykovski*, 2001]. The particle number distribution was calculated from the volumetric distribution assuming spherical particles in the assemblage and normalizing by the width of each logarithmically spaced size bin.

During times of enhanced critical angle scattering, bubble size distributions were obtained from the LISST by removing the background particle size distribution from the total particle distribution. A power law approximation was fit to the bubble size distribution data, such that:

$$n(a) = N_0 a^{-\xi} \tag{2}$$

[*Buonassissi and Dierssen*, 2010]. The equivalent spherical particle radius, a, is a nondimensional ratio of the actual particle size to a_0, where a_0 equals 1 μm. The dimensionless ξ is the exponent, also referred to as the bubble size distribution slope. The concentration factor, N_o, is the bubble differential number concentration at a_0 (number of bubbles per cubic meter per micron radius increment). The model was fit using the least squares estimator of the log-transformed variables. Bubble concentrations below 1000 $\mathrm{m}^{-3}\,\mu\mathrm{m}^{-1}$ radius

were considered statistically undersampled and were excluded from the slope calculations. The bubble size distributions have been presented with units of number m^{-3} μm^{-1} radius. The void fraction (F), the volumetric fraction of air in water, was determined following:

$$F = \frac{4\pi}{3V} \int a^3 n(a) da \tag{3}$$

where V is the volume sampled, a is radius, and $n(a)$ is the number density of the measured size distribution. Void fractions were calculated from the measured bubble size distributions.

2.2. Measurements of the Upper Ocean Dynamics

Neutral wind speeds at the reference height of 10 m (U_{10}), were measured using an air-sea flux package deployed on the jack-staff of the ship [*Edson et al.*, 2011]. The wave frequency spectrum from 0.03 to 1.2 Hz was determined by combining measurements from a Wave Monitoring System (WaMoS II), a laser altimeter (Riegl LD-90), and a Shipborne Wave Height Meter (Tsurumi Seiki Co., LTD) [*Cifuentes-Lorenzen et al.*, 2013]. Wavefield statistics, including the significant wave height of the dominant waves (H_s) and the phase speed at the spectral peak (c_p) were determined from the measured wave frequency spectrum. Variables describing the state of the wind-wavefield, including inverse wave age or wind forcing (U_{10}/c_p) were also derived from the measured wave number and frequency spectra. For open ocean conditions, high inverse wave age values (i.e., $U_{10}/c_p > 0.82$) are considered young or developing seas, while low values (i.e., $U_{10}/c_p < 0.82$) are considered old or decaying seas. The threshold, $U_{10}/c_p \sim 0.82$, is considered mature or fully developed. Measurements of whitecap coverage were determined using high-resolution digital images.

Bubble clouds were identified in measurements of acoustic backscatter (120 kHz) over 15 m of the water column. The Acoustic Doppler Current Profiler (ADCP) collected data at high sampling frequency (2 Hz) in 75 bins, each measuring 25 cm. The portion of the signal attributable to bubbles, referred to as the acoustic backscatter anomaly, was determined by the removal of the mean signal of backscatter known to be bubble free. The ADCP was deployed on a drifting, autonomous MAPCO$_2$ Buoy. Bubble measurements collected acoustically and optically were coincident in time, however they were not collocated. Here, open ocean conditions with an unlimited fetch and relatively constant wind direction supported the assumption of spatial homogeneity in the physical conditions within a mesoscale range.

Bubble penetration depths, obtained from measurements of acoustic backscatter anomaly, and the associated wind and wave conditions were compared to those reported by *Thorpe* [1992] for consistency. *Thorpe* [1992] presented the scaling of bubble plume penetration depth (d_0) to the dominant wavelength at the spectral peak (λ_p). *Thorpe* [1992] considered the values of d_0/λ in the context of the forcing using inverse wave age, where, for U_{10}/c_p of 0.6 to 2, d_0/λ ranges from 0.04 to 0.2. This approach was based on the spectral peak of the wavefield. For older seas ($U_{10}/c_p < 0.82$), breaking in the spectral peak is minimized and displaced toward higher frequencies, within shorter, steeper waves [*Terray et al.*, 1996; *Babanin et al.*, 2007; *Gemmrich et al.*, 2008; *Banner and Morison*, 2010]. Consequently, the characteristic wave scale was used in order to delineate the wind-wave region of the spectra. This scale was used in the dispersion relation for deep water waves to retrieve the mean characteristic wavelength, λ_w [*Cifuentes-Lorenzen*, 2013]. These values were compared to the d_0/λ of 0.04–0.2 (for $0.6 \leq U_{10}/c \leq 2$) reported by *Thorpe* [1992]. Ultimately, the wind and wave statistics used here could be used in future studies to estimate bubble penetration depths.

2.3. Extrapolation of the Bubble Size Distribution to a Shallower Depth

Bubble size distributions near the base of the bubble plumes (≥ 5 m) were measured as a part of this study. Bubble number concentration, for each radius increment, decays exponentially with depth [*Thorpe*, 1982; *Woolf*, 1997] and the void fractions measured at 6–9 m are very small (generally $\leq 10^{-8}$). The bubble size distributions measured here were extrapolated to shallower depths to assess the potential contribution of the small bubbles ($a < 60$ μm) to the void fraction and gas transfer processes. The SO GasEx bubble size distributions were extrapolated to 4.1 m using the observations of *Terrill et al.* [2001]. The *Terrill et al.* [2001] measurements were collected under wind and wave conditions ($U_{10} = 15$ m s^{-1}; $H_s = 3.2$ m) comparable to this study at a location in the North Pacific near Point Conception, CA. The depth and radius-dependent size distribution $N(a, z)$ is defined as:

$$N(a,z) = n(a)g(z) \tag{4}$$

In equation (4), $n(a)$ is the radius-dependent power law distribution (equation (2)) and $g(z)$ is the exponential decay behavior of the bubble size distribution with depth defined by *Woolf* [1997] as:

$$g(z) = e^{-z/L} \tag{5}$$

Here, z and L are the depth and attenuation depth (in meters), respectively. The attenuation depth (L) is the decay rate of the bubble concentration with depth. The functional behavior of the bubble size distribution with depth is determined using:

$$N(a,z) = Ba^{-\xi}e^{-z/L} \tag{6}$$

where B is a coefficient of proportionality. Assuming a constant size distribution slope, ξ, a solution for B was determined from

$$N_i = B_i e^{-z_i/L} \tag{7}$$

where $i = 1$ is the SO GasEx bubble size distribution and $i = 2$ is the *Terrill et al.* [2001] bubble size distribution. The value for L was selected so that continuity between the *Terrill et al.* [2001] data and the SO GasEx extrapolated bubble size distribution was achieved. A length of approximately 1 m is typical [*Thorpe*, 1986; *Woolf and Thorpe*, 1991; *Woolf*, 1997]. The bubble size distributions measured here were not extrapolated above $1/2H_s$, where extrapolations are likely no longer valid [*Baldy*, 1988].

3. Results

Measurements were conducted from yearday 69 to 92, at stations north of South Georgia Island in a region characterized by moderate phytoplankton biomass and high wind conditions. The majority of stations were sampled on the eastern edge of a high chlorophyll (0.4–1 mg m^{-3}) patch at latitude 51°S, as shown in the satellite-derived average chlorophyll imagery for March 2008 (Figure 1). From yearday 75 to 77, stations were sampled 300 km further south at latitude 54°S in waters surrounding South Georgia Island. Wind speed throughout the experiment varied from <1 to 20 m s^{-1} [*Edson et al.*, 2011]. This study focuses on bubble measurements made during periods of high wind speeds ($U_{10} \approx 13$ m s^{-1}) recorded on yeardays 76, 80, and 84. Two stations measured during low wind conditions ($U_{10} \approx 3$–5 m s^{-1}) on yeardays 81 and 86 were used as control stations (Figure 2).

3.1. Optical Measurements of Bubbles

During the days with high wind speeds of approximately $U_{10} \approx 13$ m s^{-1} (yeardays 76, 80, and 84), bubbles were detected at 6–9 m in both optical and acoustical measurements. Measurements of the angular scattering of light, the VSF from 10° to 170°, confirm the temporary presence of bubbles with enhanced scattering at the critical angle, $\beta(80)$ (Figure 3). Figures 3a, 3c, and 3e show the change in the shape of 1 Hz averaged VSF measurements throughout the 30 min time series for the three stations experiencing high wind conditions. The normalized VSF data averaged to 1 Hz are also shown on a two-dimensional plot to emphasize the magnitude of the increase in critical angle scattering (Figures 3b, 3d, and 3f). To evaluate the relative angular shape of the VSF, each measured VSF was normalized to the mean of the time series at each angle. Hence, a value of 1 is expected for each angle when the VSF is similar to the mean VSF in the water column. For all three stations, enhancements of more than twofold to threefold in critical angle scattering occurred periodically throughout the 30 min deployment. Other changes in the VSF shape also occurred, including enhancements in backscattering (90°–170°), sometimes by more than a factor of 2, during bubble events (Figures 3b, 3d, and 3f). Mie modeled scattering suggests the small peak present in the VSF occurring near 130° is likely caused by the presence of particulate material with a relative refractive index of approximately 1.20, similar to calcite [*Zhang et al.*, 2002]. According to *Balch et al.* [2011], coccolithophores and coccoliths were present and contributed 1–23% of the total backscattering at these stations.

Critical angle enhancements in the VSF were not observed during the low wind conditions, as illustrated by Figure 4. The measurements of the VSF collected during high wind speed conditions on yearday 84
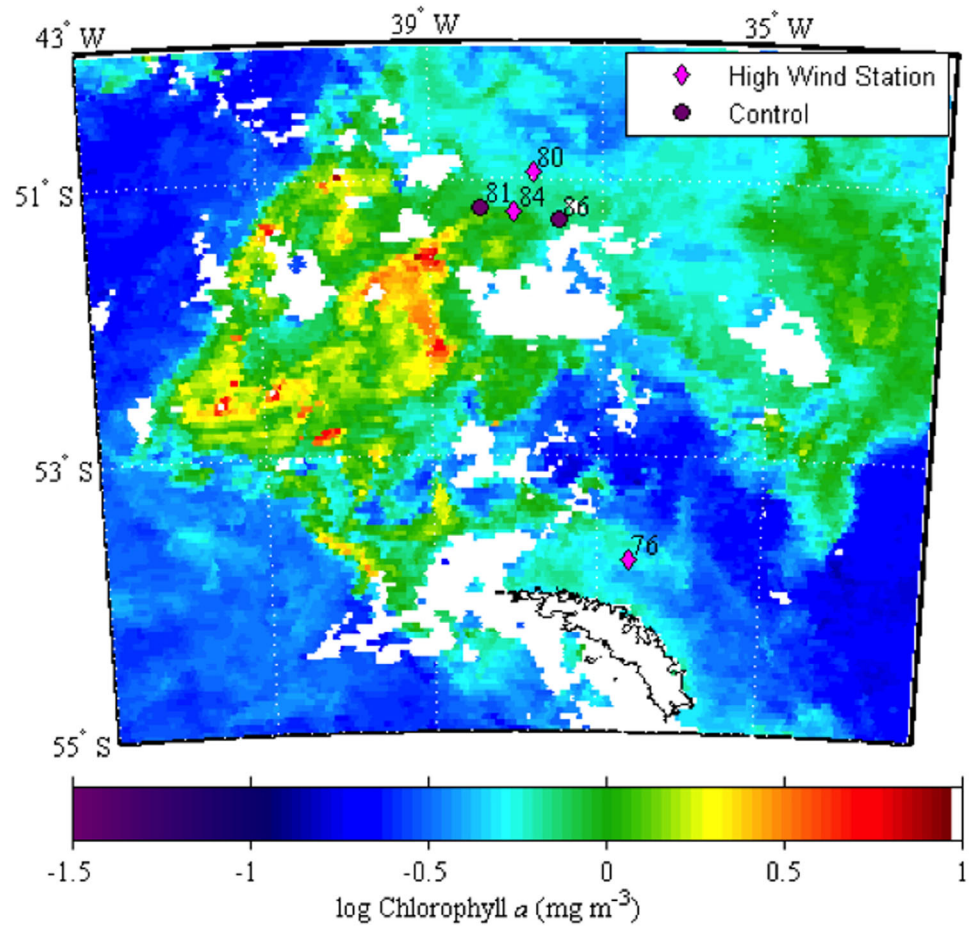
Figure 1. South Atlantic sampling region and station locations (labeled with the yearday) overlayed on the satellite-derived average chlorophyll a (mg m^{-3}) from the MODIS Aqua sensor (nominal 4 km resolution) for the month of March 2008. Three stations were sampled during high wind conditions (pink diamonds) and two were sampled during low wind conditions (purple circles). The white patches in the image indicate areas with no data due to cloud cover.
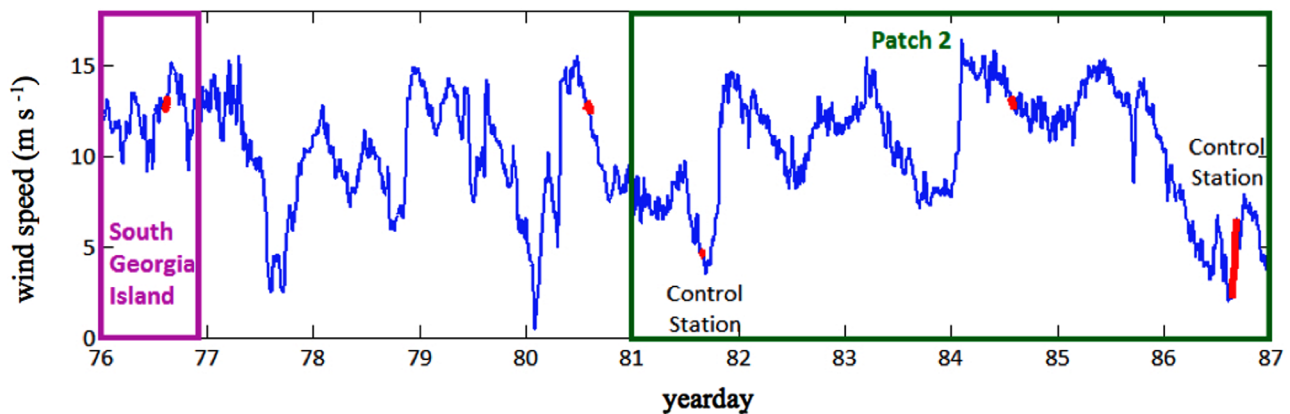

Figure 2. The wind speed record for SO GasEx, where the red highlighted regions identify the ≈30 min time periods during which the bubble data were collected. The mean wind speed (U_{10}) from each sampling period is reported in Table 1. The wind speed stayed relatively constant for all stations during sampling except on yearday 86, during which the wind speed increases by 3 m s^{-1} (red line). Day 80 and stations within Patch 2 (green box) correspond to 50.6°S, 38°W. Time before Patch 2 was spent approximately 300 km north of South Georgia Island (53.8°S, 36.6°W).
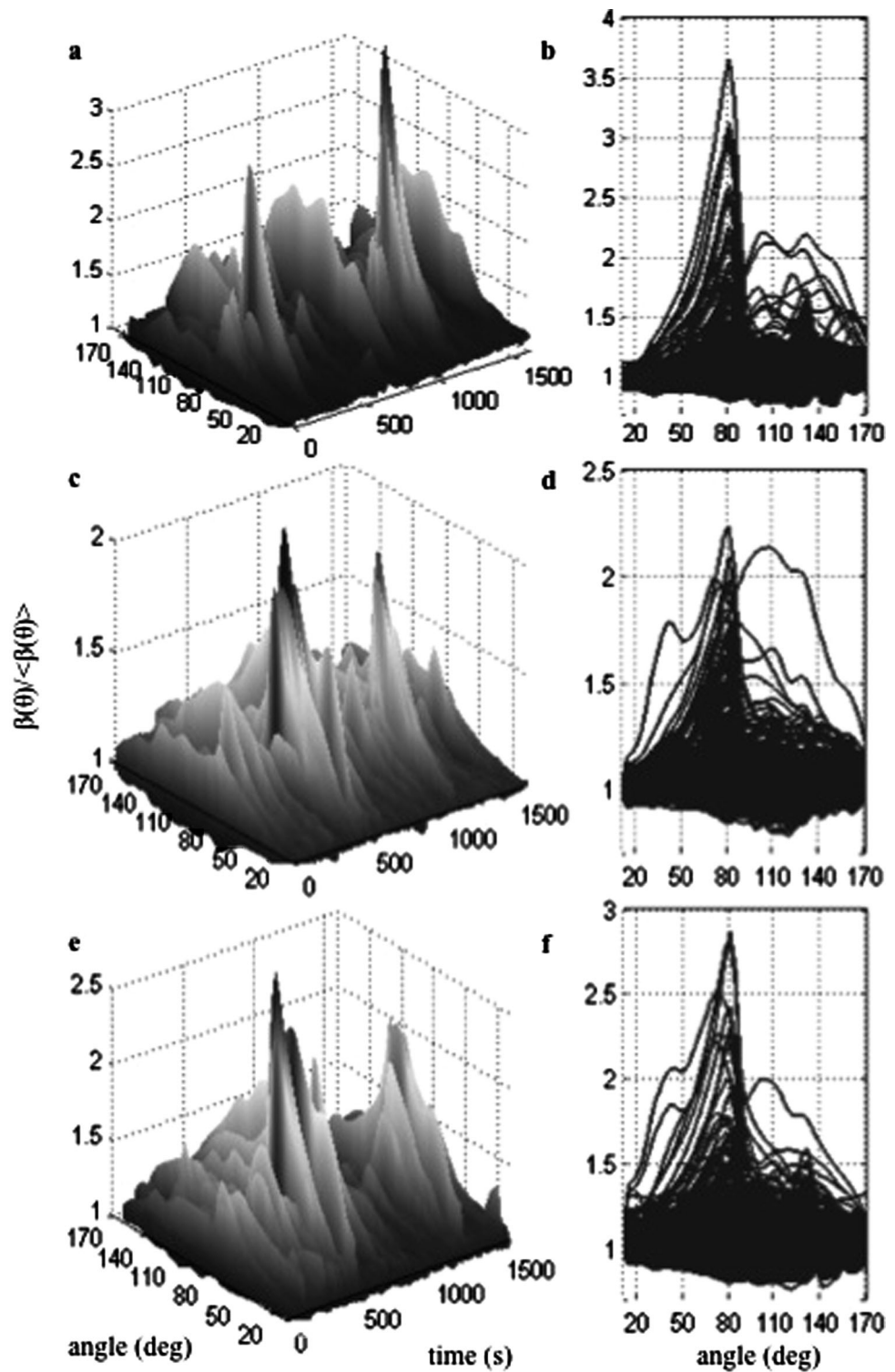
Figure 3. High-frequency (1 Hz) time series measurements of the mean normalized volume scattering function (VSF) for the three stations in the Southern Ocean measured during periods of high wind ($U_{10} \sim 13$ m s^{-1}) on yeardays (a) 76, (c) 80, and (e) 84 show temporary (75–180 s) enhancements in scattering at several angles. The most pronounced temporary enhancements occur at and around the critical angle scattering angle ($\sim 80°$), due to bubble entrainment. The temporary enhancement in scattering in the backward direction (measured from 90° to 170°) is also apparent. (b, d, and f) The same data as in Figures 3a, 3c, and 3e, but replicated on a two-dimensional axis in order to more easily evaluate the magnitude of critical angle scattering at 80°. Enhancements of twofold to threefold occurred periodically throughout the 30 min deployments at all three stations (Figures 3b, 3d, and 3f).
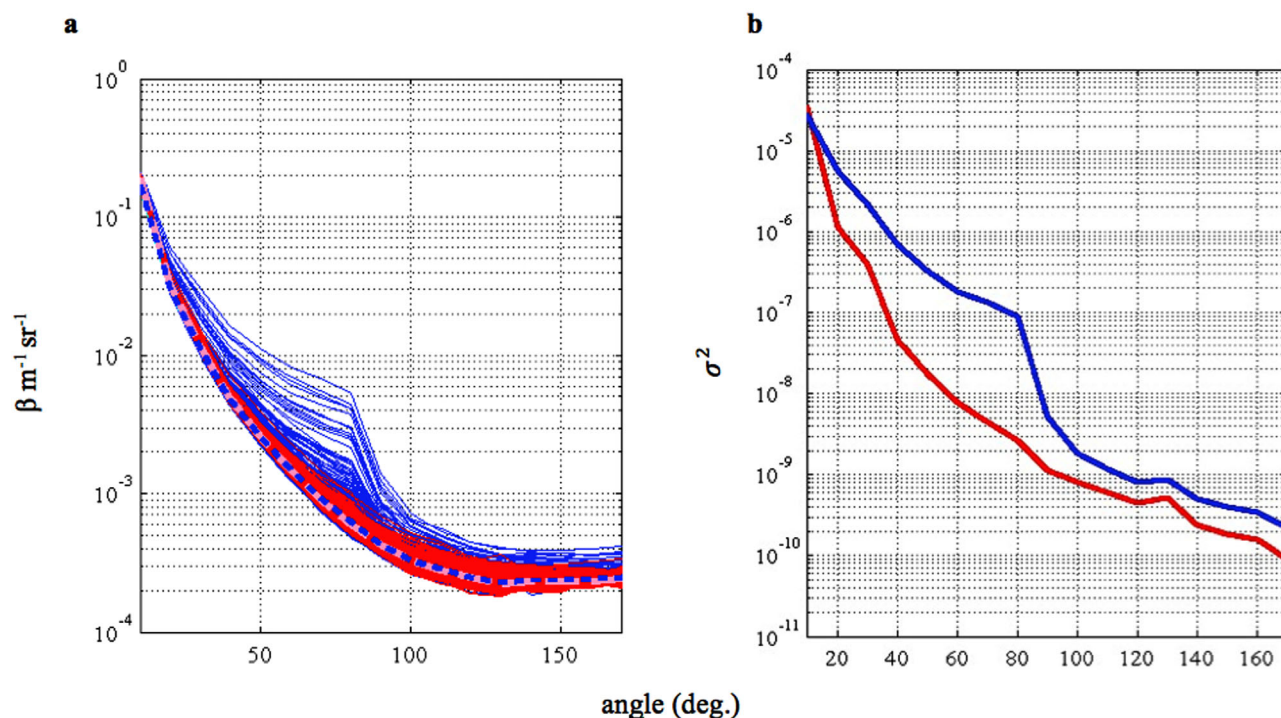
Figure 4. (a) MASCOT measured full VSF collected at a 1 Hz sampling frequency (each line represents the 1 Hz data) during periods of high (yearday 84; $U_{10} \approx 13$ m s^{-1}, blue lines; mean is blue dashed line) and low (yearday 86; $U_{10} \approx 3$ m s^{-1}, red lines; mean is pink dashed line) wind conditions for stations with similar particulate populations and background optical properties. (b) The variance of the high-frequency VSF time series collected during the periods of high (blue line) and low (red line) winds are plotted as a function of angle. Relative to the variance of the VSF time series collected during low wind conditions (red), the variance of the VSF collected during high wind conditions (blue) is enhanced at all angles. The variance of the VSF at the critical angle (80°) is approximately 2 orders of magnitude higher during periods of high wind relative to periods of low wind.

($U_{10} = 13$ m s^{-1}; Figure 4, blue lines) were compared to the VSF measurements collected during low wind conditions on yearday 86 ($U_{10} = 3$ m s^{-1}; Figure 4, red lines). Each line represents a VSF collected at a sampling frequency averaged to 1 Hz. These two stations had similar water column properties and amounts of total suspended material and chlorophyll *a*, but were sampled under markedly different wind and wave conditions. As expected, the VSF measured during low wind conditions showed no enhancement in scattering at the critical angle. Instead, a conventional oceanic VSF, with large amounts of light scattered in the forward direction (10°–90°) and less than 3% of the light scattered in the backward direction (90°–180°) was observed. Such VSFs, declining smoothly from 90° to 180°, are found throughout the world's oceans [*Sullivan and Twardowski*, 2009] and are used in radiative transfer modeling [*Fournier and Forand*, 1994; *Mobley et al.*, 2002]. In contrast, the VSF measured at stations experiencing high wind conditions showed an enhancement in scattering across all angles and at the critical angle in particular when bubbles were present (Figure 4, blue lines).

Moreover, the VSF at the critical angle $\beta(80)$ measured over the time series followed a different statistical distribution for the low and high wind stations. The low wind data are nearly lognormally distributed (Figure 5a, dotted line) and centered at the mean value of 5.5. In contrast, $\beta(80)$ data collected during high wind conditions were not normally distributed, but closely followed a Generalized Extreme Value (GEV) type II (or Fréchet) distribution (Figure 5a). For these stations, the central tendency is similar, but the tail shape parameter k, were heavily positively skewed ($0.24 < k < 0.32$) due to the intermittent presence of bubbles (Figure 5a, dashed lines). The variance of critical angle scattering collected during yeardays 76, 80, and 84 was also much higher ($3.7 \times 10^{-9} \leq \sigma^2 \leq 1.2 \times 10^{-8}$) relative to the control ($\sigma^2 = 7.2 \times 10^{-10}$). For yeardays 76, 80, and 84, 16% 12%, and 21% of the critical angle scattering measurements exceeded the range of the control (Figure 5b, dashed lines).

Various measurements indicate the presence of sufficient dissolved organic material to coat bubbles. Absorption by colored dissolved organic matter at 412 nm ranged from 0.03 to 0.1 m^{-1}. Globally
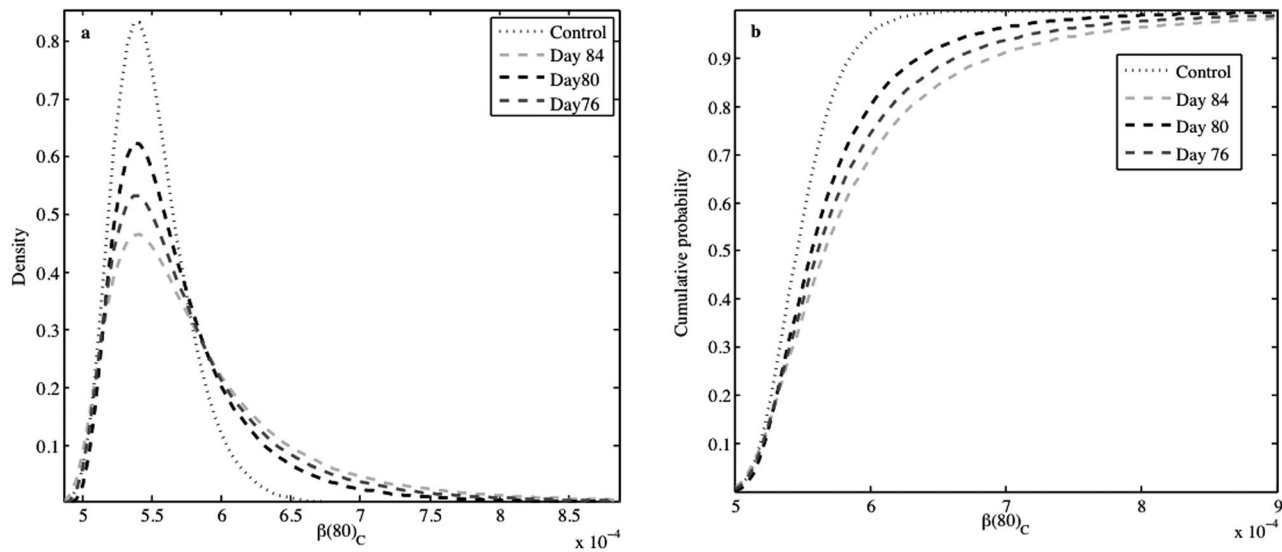
Figure 5. (a) The probability density distribution of critical angle scattering normalized by the cumulative sum of $\beta(80)$ for each station ($\beta(80)_C$), for stations experiencing high wind conditions, yeardays 84 (light gray, dashed line), 80 (black, dashed line), and 76 (dark gray, dashed line) compared to the mean of the control stations experiencing low wind conditions (control, dotted line). (b) The cumulative probability distribution of $\beta(80)$ for stations experiencing high wind conditions, yeardays 76, 80, and 84 (dashed lines), showed 16%,12%, and 21% of critical angle scattering measurements exceeded the range of the control (dotted lines), respectively. The variance of critical angle scattering collected during yeardays 76, 80, and 84 was high ($3.7 \times 10^{-9} \leq \sigma^2 \leq 1.2 \times 10^{-8}$) relative to the control ($\sigma^2 = 7.2 \times 10^{-10}$).

representative values of colored dissolved organic matter for comparison, including coastal values, fall within the range of 0.003–10 m^{-1} [*Twardowski et al.*, 2004]. Similarly, discrete measurements of total and dissolved organic carbon during SO GasEx were within the range of 56–72 µM and 50–76 µM, respectively (P. Vlahos, personal communication, 2009). These concentrations are consistent with those used in the analysis of *Detwiler and Blanchard* [1978], for which bubbles became coated within 5 s of entrainment.

3.2. Measurements of the Bubble Size Distribution

The LISST measured bubble size distributions ranged from 0.5 to 125 µm radius; however, no bubbles with greater than 60 µm were detected at the depth of measurement (Figure 6). Bubble injections occurred on all days during which high winds were measured and the events typically lasted from tens to over a hundred seconds in duration. The shaded regions in Figure 6 represent the range in the bubble size distribution records averaged to a 1 Hz sampling frequency. The lines represent the mean and standard deviation of the bubble size distribution for each bubble event. On yearday 76, two bubble events occurred 13.5 min apart and lasted 150 and 180 s in duration. Similarly, on yearday 80 two distinct bubble events lasting 160–180 s in duration were measured. The most dense and intense bubble events were measured on yearday 84. The first event produced a 10-fold increase in critical angle scattering lasting 75 s in duration. A second isolated event occurred 5 min later, lasting 140 s in duration. Finally, the time series ended with a seemingly long period (512 s), during which the VSF fluctuated from high to low critical angle scattering. It is possible that these bubbles are part of a large plume that is being advected past the instrument package or that the bubbles are being recirculated. Alternatively, bubbles measured during this event could be part of a larger bubble plume than the other plumes measured. The background particulate population within the size range measured by the LISST did not change significantly over the course of the 30 min time series on any of the stations.

A power law was fit to each 1 Hz bubble size distribution spectrum over the size range sampled for which bubble populations exceed 10^3 m^{-3} µm^{-1} between 2 and 40 µm (Table 2). Though the use of a power law fit is simplistic and offers only a first-order approximation [*Buonassissi and Dierssen*, 2010], it is commonly used to describe bubble size distributions [i.e., *Medwin*, 1977; *Vagle and Farmer*, 1992; *Woolf*, 1997]. Mean slopes, ξ, for the bubble size distributions collected on yeardays 76, 80, and 84 were 4.6, 4.1, and 3.6, respectively. A range in measured slopes, generally 2.9–5.1, was measured throughout the lifetime of the bubble events. A number of fine-scale features are apparent in the measured bubble size distributions and could be associated with uncertainties in the measurements. For example, a change in the slope occurs between
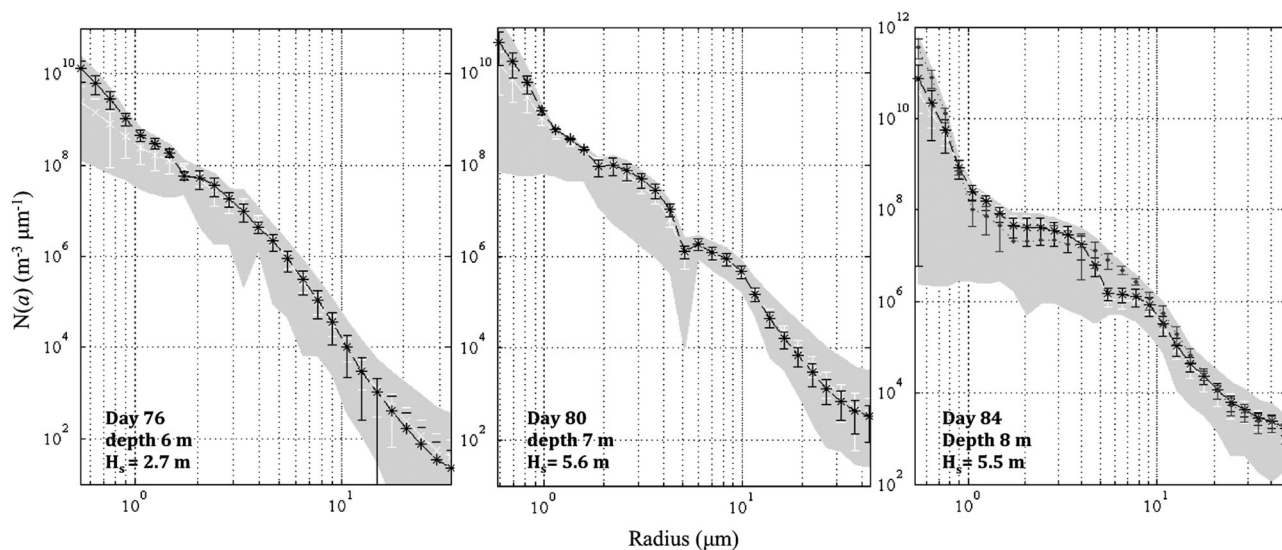
Figure 6. Bubble size distributions measured with the LISST instrument during high wind conditions ($\approx$13 m s^{-1}) on yeardays (a) 76, (b) 80, and (c) 84. The shaded region represents the range in the BSD records collected at 1 Hz sampling frequency. The lines represent the mean and standard deviation of the BSD for each bubble event. (a) On yearday 76, two bubble events occurred 13.5 min apart and lasted 150 (black asterisk) and 180 s (white x) in duration. (b) On yearday 80, two distinct bubble events lasting 160 (black asterisk) to 180 s (white x) in duration were measured. (c) Three events occurred on yearday 84. The first two lasted 75 s (black asterisk) and 140 s (white x) in duration. The time series ended with a seemingly long (512 s) event, during which the VSF fluctuated from high to low critical angle scattering. The range in bubble size distribution slope, depth of measurement, and oceanographic conditions are reported in Table 2 for each station.

1 and 2 μm radius, such that small bubbles followed a shallower slope and large bubbles, a relatively steeper slope. Very steep slopes for the smallest size classes ($0.5 \leq a \leq 1$ μm) could be an artifact of the measurement where "rising tails" in the distribution can be produced by stray light, irregularly shaped, or submicron particles [*Agrawal and Pottsmith*, 2000; *Buonassissi and Dierssen*, 2010; *Andrews et al.*, 2011]. The LISST inversion method is still being refined, therefore the uncertainty associated with the fine-scale dips and peaks in the size distribution and the accuracy of such features are being considered in future research. However, it is also possible that the discontinuities in the power law slope of the bubble size distribution could be delineating lognormally distributed subpopulations of bubbles with different temporal and spatial dynamics [see *Zhang et al.*, 2011; *Czerski et al.*, 2011; *Twardowski et al.*, 2012].

A comparison between the bubble size distributions presented here and previously published size distributions [i.e., *Johnson and Cooke*, 1979; *Farmer and Vagle*, 1989; *Breitz and Medwin*, 1989; *Phelps and Leighton*, 1998; *Pascal et al.*, 2010] shows a general consistency in the size distribution shape, except for the absence of the peak that appears in many published bubble size distributions (Table 3; Figure 7 adapted from *Brooks et al.* [2009]). The average slopes of the size distributions measured in the Southern Ocean were slightly steeper (mean $\xi = 4.6$, 4.1, and 3.61) than the majority of the published slopes ($\xi \sim 3$–4). Also, substantial differences in the magnitude of bubble concentration were observed between bubbles measured here and those presented in previously published research within the radius range of 10–25 μm (the size classes included in all of the plotted bubble size distributions).

The small bubbles sizes measured at 6–9 m depth during SO GasEx yielded void fractions $O(10^{-8}-10^{-7})$, whereas bubble populations near the surface typically correspond to void fractions $O(10^{-4})$ (Table 2). The volume contribution of air by the smallest size classes ($a < 10$ μm) was not negligible. As small bubbles were incrementally included in the integration from large to small sizes, the total void fraction continued to increase, though at a lower rate relative to that contributed by larger ($a > 10$ μm) bubble sizes (Figure 8). Exclusion of the smallest bubbles in the calculation of the total void fraction would ultimately result in an order of magnitude underestimation.

3.3. The Evolution of Bubble Events
The evolution of the bubble population during events was investigated in the 1 Hz data collected using the LISST. As a result of the wave conditions, the optical instruments were not held at a fixed depth for the
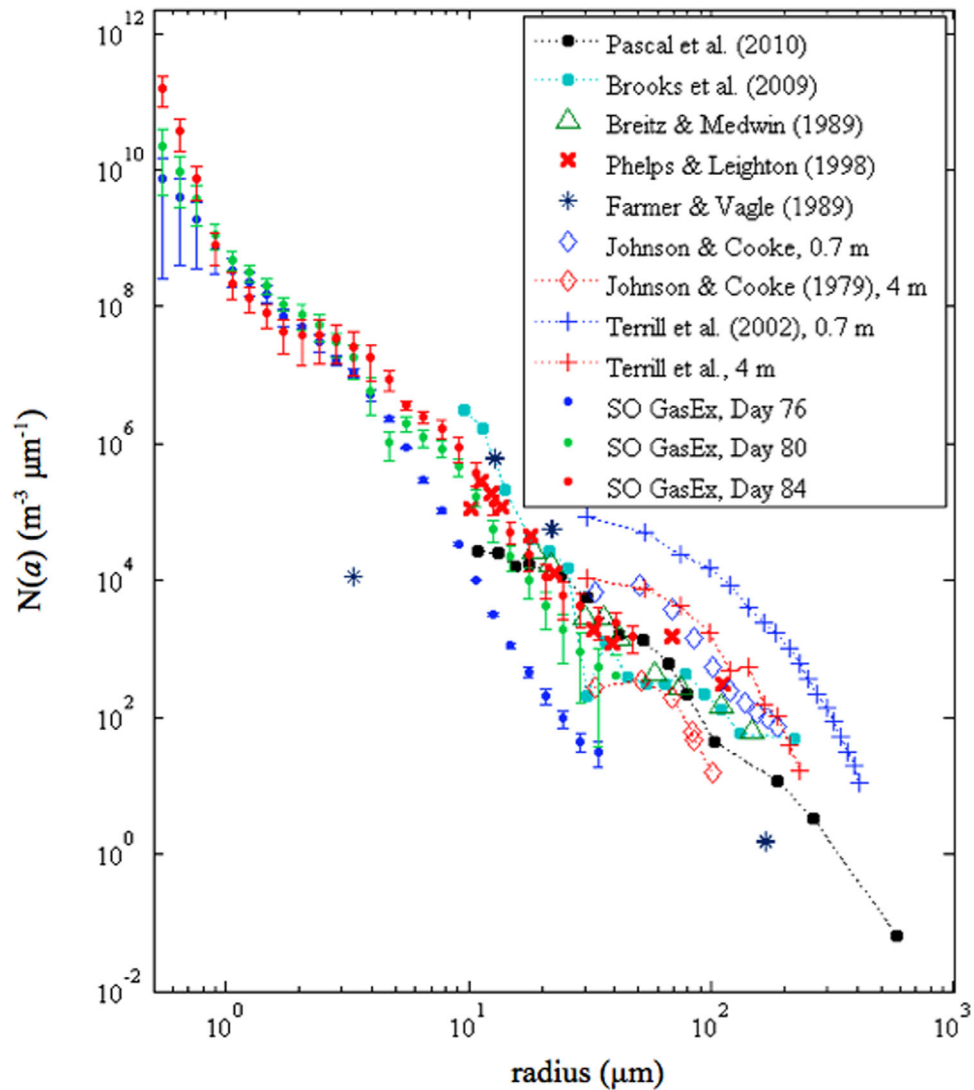
Figure 7. Adapted from *Brooks et al.* [2009]. A comparison between mean and standard deviation of the bubble size distributions from SO GasEx collected on yeardays 76 (blue), 80 (green), and 84(red) to those by *Breitz and Medwin* [1989] (triangles), *Johnson and Cooke* [1979] (diamonds), *Phelps and Leighton* [1998] (x's), and *Farmer and Vagle* [1989] (asterisks). Also included are the BSDs measured during DOGEE [*Pascal et al.*, 2011] (black dots) and the UK-SOLAS SEASAW (blue dots) projects. See Table 3 for the oceanographic conditions, measurement techniques, and locations associated with the previously published BSDs shown.

duration of the time series. In order to account for this, the data were bin averaged based on the peak frequency of the pressure measurement collected by the LISST. For yeardays 76, 80, and 84, the peak frequency of package motion followed the period of the swell and occurred at 0.172, 0.106, and 0.094 Hz, corresponding to periods of 5.8, 9.4, and 10.7 s, respectively. Both the bubble number concentration and the size distribution changed throughout the evolution of the bubble event until the bubble cloud was no longer detectable, at which time scattering at the critical angle and the concentration of particles returned to background levels. However, no statistically significant trend in the composition of the bubble population (i.e., steepening or flattening of the bubble size distribution) was found throughout the evolution of the bubble events (Figure 9).

3.4. Bubble Measurements in the Context of Wind and Wave Dynamics

During moderate to high wind conditions (up to 19 m s^{-1}), large-scale wave breaking and bubble entrainment was observed during the course of the experiment. Figure 10 shows the time series record of wind speed (white line) and acoustic backscatter anomaly (surface coloration) with depth, indicating a relatively
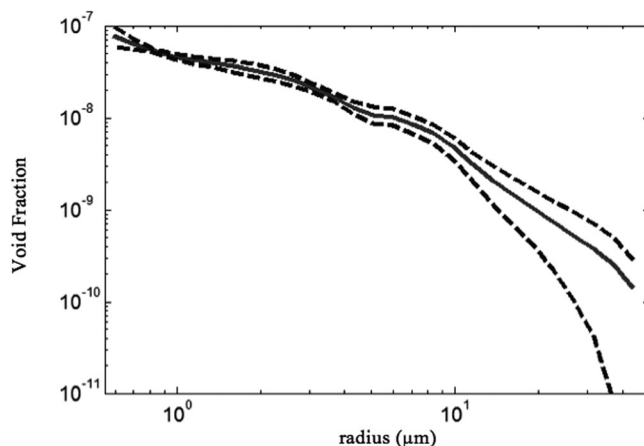
Figure 8. An example of the cumulative void fraction of air in water (dimensionless) calculated from large to small size classes for the first bubble event occurring on yearday 80, where the solid black line is the mean and the dashed gray lines denote one standard deviation above and below the mean.

stable subsurface bubble layer. An acoustic backscatter anomaly of 0 indicated water devoid of bubbles and a high value indicated dense bubble plumes.

Differences exist between the bubble size distributions measured at each station due, in part, to the prevailing physical forcing conditions (Table 1). No statistical relationships can be investigated between the bubble populations and environmental conditions measured here due to the limited number of stations. However, the physical conditions associated with the measured bubble populations were reported to aid in both the interpretation of the observed bubble events and in identifying the locations of measurements within the bubble plumes.

The prevailing physical forcing conditions during yeardays 80 and 84 were similar. The mean significant wave height and inverse wave age measured on yeardays 80 and 84 were 3.8 and 3.4 m and 0.73 and 0.64 (Table 1). Large breaking events under strong wind forcing led to the vertical extension of bubble plumes deep into the surface water column on yearday 84. Measurements of the acoustic backscatter anomaly identified bubble penetration depths of up to 15 m, with a high intensity range occurring between the surface and 6 m (Figures 11a and 11c). The mean penetration depth normalized by the characteristic wavelength (λ_w) for yearday 84 was 1.12 (Table 2). A bubble plume penetration depth ranging from 7.7 to 11.6 m was estimated for yearday 80, assuming the normalized penetration depth scaling from yeardays 76 and 84. The longer characteristic wavelengths measured on these yeardays (λ_w of 9.7 and 10.6 m) resulted in more intense plumes with a slowly decaying mean bubble radius with depth relative to yearday 76 (Table 1). During yeardays 80 and 84, bubbles as large as 50 μm in radius were measured.
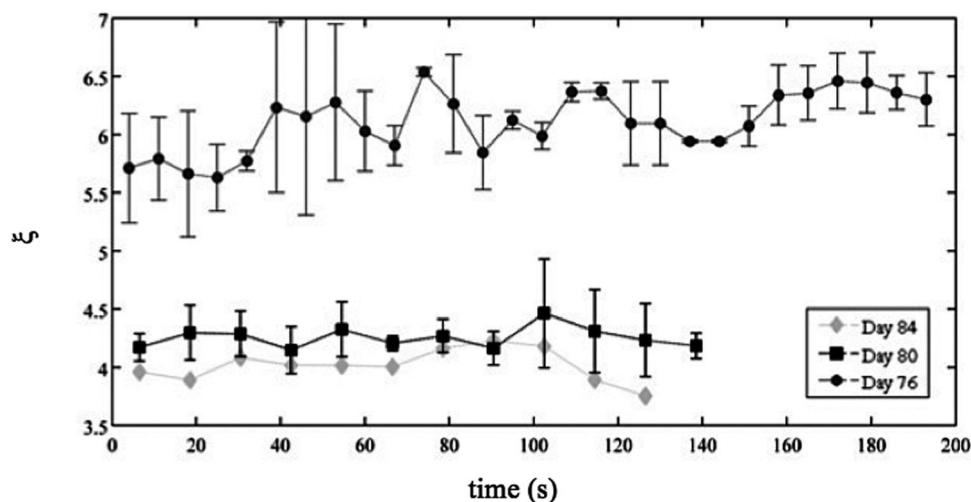

Figure 9. The bubble plume evolution was traced through time using the power law slope fit to the low-pass filtered BSDs from 5 to 30 μm (ξ'). The time-dependent ξ' for all events at each station were averaged to analyze trends in the bubble size distribution throughout bubble events. The error bars are standard deviations. The average of the two bubble events occurring on yearday 76 showed a slight increasing trend over time (gray circles), whereas bubble events on yeardays 80 (2 events, black squares) and 84 (1 event, gray diamonds) showed no significant trend over time.
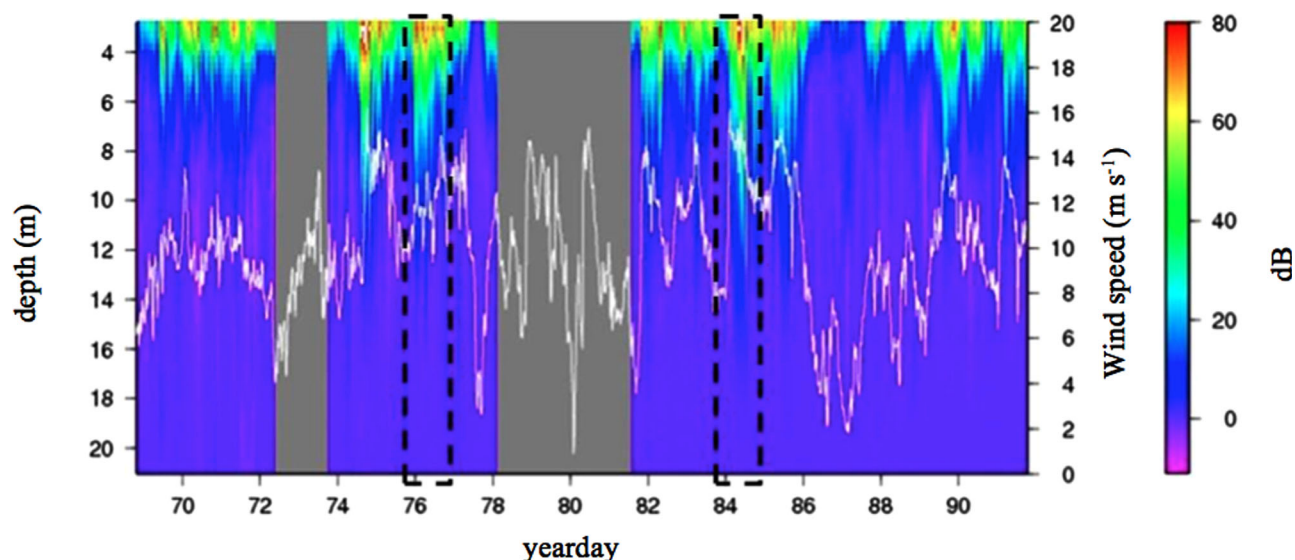
Figure 10. Acoustic backscatter anomaly (dB) and wind speed record (white line) for the SO GasEx experiment. The acoustic backscatter anomaly is a measure of the density of bubbles within the water column, where a high acoustic backscatter anomaly corresponds to dense bubbles. An acoustic backscatter anomaly of 0 means no bubbles are detected. The periods of high winds, yeardays 76 and 84, are identified with black dashed boxes. The gray box indicates the time period during which no acoustic data were collected (i.e., yearday 80).

Smaller significant wave height (H_s = 2.8 m) and shorter characteristic wavelength (λ_w = 5.8 m) measurements were observed on yearday 76. This resulted in lower intensity bubble clouds at depth and maximum bubble sizes that did not exceed 30 μm in radius. The most intense breaking events observed on yearday 76 produced penetration depths exceeding 10 m. However, bubble plumes generally did not extend beyond 5 m (Figures 11a and 11b). The mean normalized penetration depth (d/λ_w) measured during yearday 76 was 0.90 (Table 2).

3.5. Extrapolation of the Bubble Size Distribution to Shallower Depths

The discrepancies in concentration and slope between the bubble size distributions measured here and previously published bubble size distributions are likely due to the depth of measurement. Between 6 and 9 m, few bubbles larger than 50 μm radius were measured. Measurements of the acoustic backscatter anomaly (dB) suggest that the bubble size distributions collected in the Southern Ocean are at the base of plumes (Figure 10), consistent with the result of fewer bubbles and steeper size distribution slopes. An extrapolation of the SO GasEx bubble size distribution was completed to estimate the contribution of small bubbles to the void fraction at a shallower depth. The mean bubble size distribution measured at 6–9 m in the Southern Ocean was extrapolated to a depth of 4.1 m using a power law fit to the SO GasEx and *Terrill et al*. [2001] bubble size distributions (equation (2)) and equations (5–8). An attenuation depth (L) of 1.2 m was assumed in order to guarantee continuity between the *Terrill et al*. [2001] and SO GasEx bubble size distributions at 4 m. This attenuation depth is consistent with the wind speed relationships presented by *Woolf* [1997] and *Thorpe* [1992] and with measurements presented by *Vagle et al*. [2010]. The power law fit to the SO GasEx and *Terrill et al*. [2001] data yielded N values of 3.39×10^9 and 2.44×10^9 and ξ values of 4.1 and

Table 1. A Summary of the Physical Conditions Measured at Five Southern Ocean Stations Including the Mean Neutral Wind Speed (at 10 m) for the Sampling Period (U_{10}, m s^{-1}), Mean Sea Surface Temperature at 5 m (T_w, °C), Mean Air Temperature at 10 m (T_{air}, °C), Mean Measured or Estimated Fractional Whitecap Coverage (WC), Mean Significant Wave Height (H_s, m), Mean Peak Phase Speed (c_p, m s^{-1}), Range of the Inverse Wave Age (U_{10}/c_p), and Mean Characteristic Wavelength (λ_w, m) Based on the Characteristic Phase Speed

Day of Year	U_{10} (m s^{-1})	T_w (°C)	T_{air} (°C)	WC	H_s (m)	c_p (m s^{-1})	U_{10}/c_p (range)	λ_w (m)
76	12.8	3.3	4.6	0.006	2.8	14.2	0.55–1.13	5.8
80	12.7	5.7	7.7	0.002[a]	3.8	19.2	0.52–0.80	8.5
84	13.0	4.9	2.2	0.030	3.4	16.9	0.46–0.85	7.0
86 Control	3.1	4.8	5.1	0.001	2.7	17.1	0.15–0.72	3.6
81 Control	4.6	5.1	6.0	0.001[a]	3.4	14.1	0.10–0.80	3.7

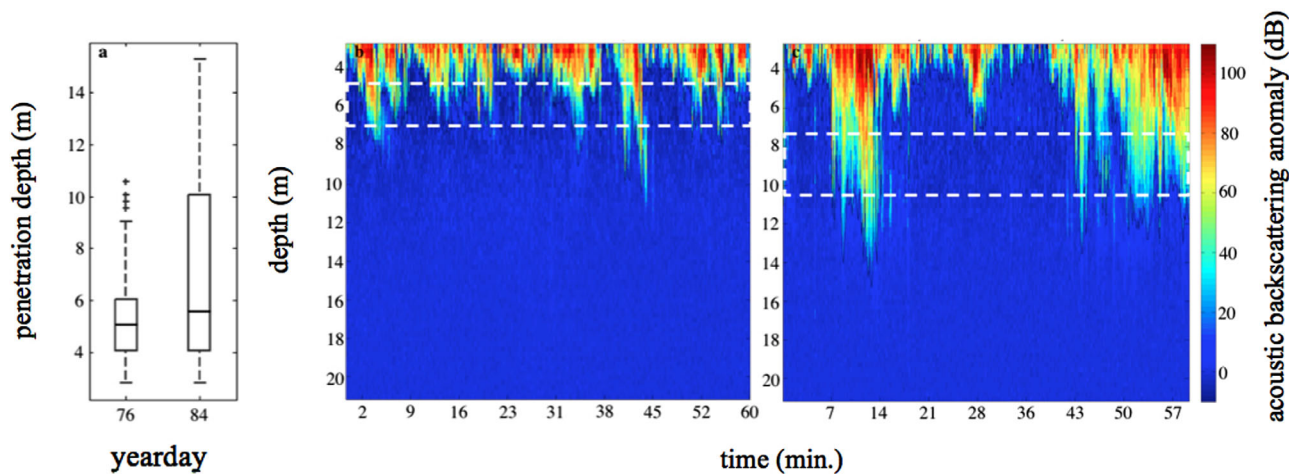[a]Estimated based on wind speed following *Monahan and Spillane* [1984].

Figure 11. (a) Bubble plume penetration depths estimated using time series measurements of acoustic backscatter anomaly (dB) collected on yeardays, (b) 76, and (c) 84. In Figure 11a, the box denotes the lower quartile, median, and upper quartile penetration depth values. The whiskers show the range of the data and the pluses denote outliers. High temporal resolution plots of the acoustic backscatter anomaly over the 1 h sampling period show intense breaking on (a) yeardays 76 and (b) 84 days produced bubble plumes that extended to 10 and 15 m, respectively. No acoustic data were collected on yearday 80.

3.3, respectively. The depth-dependent bubble size distribution $n(a, z)$ in the range of 8–4 m was given in a stepwise manner following:

$$n(a,z) = \begin{cases} B_1 a^{-\xi_1} e^{-z/L}, & 2 \leq a \leq 30 \ \mu m \\ B_2 a^{-\xi_2} e^{-z/L}, & 30 < a \leq 120 \ \mu m \end{cases} \tag{8}$$

where B_1 and B_2 are coefficients of proportionality determined using equation (7) (Figure 12). The full ($2 \leq a \leq 120 \ \mu m$), *Terrill et al.* [2001] derived SO GasEx bubble size distribution at 4 m produced a total void fraction of 9.8×10^{-7}. Bubbles $30 < a \leq 120 \ \mu m$ in size contributed 6.3×10^{-7} and the smallest bubbles, $2 \leq a \leq 30 \ \mu m$, contributed 3.5×10^{-7} to the total void fraction.

3.6. The Contribution of Bubbles to Dissolved Oxygen

Supersaturations of up to 5% were measured during high wind conditions in the Southern Ocean. Using the model of *Woolf and Thorpe* [1991] and *Moore et al.* [2011] estimated the bubble-mediated contribution to O_2 supersaturation to be 1%–2% at 5 m during yeardays 76 and 84, respectively. However, the model applied is based on the bubble size distribution measurements of *Johnson and Cooke* [1979] and neglects bubbles <30 μm in size (Figure 13a). *Woolf and Thorpe* [1991] refer to the exclusion of these bubbles as a serious omission because the incremental inclusion of smaller bubble sizes substantially increases the gas injection rate and the projected equilibrium supersaturation (Figure 13b, black dots). The supersaturating effect of bubbles during high wind conditions (i.e., 13 m s^{-1}) could exceed the estimated 1–2% and account for a larger portion of the measured supersaturation (perhaps up to 4–5%) by extending the SO GasEx bubble size distributions measured here to 1 μm (Figure 13b, gray dots).

Table 2. Bubble Size Distribution (BSD) Statistics Collected at Depth (z, m) at Three Stations Experiencing High Wind Conditions (U_{10}, m s^{-1}), Including the Mean Bubble Penetration Depth (d_0, m), the Normalized Penetration Depths (Dimensionless), Which Describe the Relationship Between Bubble Plume Penetration Depth and the Characteristic Wavelength (d/λ_w), the Mean and Range of Power Law Slopes of the BSD Extending From 2 to 40 μm Radius (ξ), the Logarithmic Concentration Factor (N_0, m^{-3} μm^{-1}), and the Mean Void Fraction (F) of all Events for Each Station

Day of Year	z (m)	U_{10} (m s^{-1})	d_0 (m)	d/λ_w	ξ ($2 < a \leq 40$) Mean (range)	BSD N_0 (m^{-3} μm^{-1})	F
76	6.0 (±1)	12.8	5.2	0.90	4.6 (4.2–5.1)	10.7	10^{-8}
80	6.8 (±1.5)	12.7	7.7–8.4[a]	Unknown	4.1 (3.9–4.3)	10.6	10^{-7}
84	8.6 (±2)	13.0	6.9	0.99	3.6 (2.9–3.8)	10.4	10^{-7}

[a]Estimated range in penetration depths based on the normalized penetration depth scaling from days 76 and 84.

Table 3. Summary of Conditions Associated With Previously Published Bubble Size Distributions Shown in Figure 14 Including the Depth of Measurement, the Mean Wind Speed ($\overline{U}_{10}$; m s^{-1}), Water Temperature (T_w; °C), a Description of the Wave Field, the Instrument Used in Measuring the BSD, and the Location at Which the Measurements Were Collected

Reference	Depth of Measurement (m)	U_{10} (m s^{-1})	T_w (°C)	Wavefield	Measurement Approach, Location
Brooks et al. [2009]	Unknown	≈14	9	$H_s \approx 2.7$	Bubble Camera
Johnson and Cooke [1979]	0.7	11–13	2	$H_s \approx 2.0$	Photographic, St. Margaret's Bay, Nova Scotia
Breitz and Medwin [1989]	0.25	12–15		3 m swell	Acoustic, Monterey Bay
Farmer and Vagle [1989]	0.10	12–14	21.5	5 s period	Acoustic, Atlantic (28°N, 70°W)
Phelps and Leighton [1998]	0.50	10–12		No data	Acoustic, South Hampton Coast ($z = 17$–22 m)
Pascal et al. [2010]	2–3	14	17	$H_s = 2.7$	Acoustic, Fiber optic, North Atlantic

4. Discussion

Concurrent optical measurements of the particle size distribution and the volume scattering of light at the critical angle were used to identify naturally occurring, transient O($10^1 - 10^2$) s, deeply penetrating bubble populations during large-scale wave breaking in the Southern Ocean. This is a very limited data set, containing only three stations for which bubble measurements were collected. No statistical analyses can be performed nor any broad conclusions made about the behavior of the bubbles measured here and their
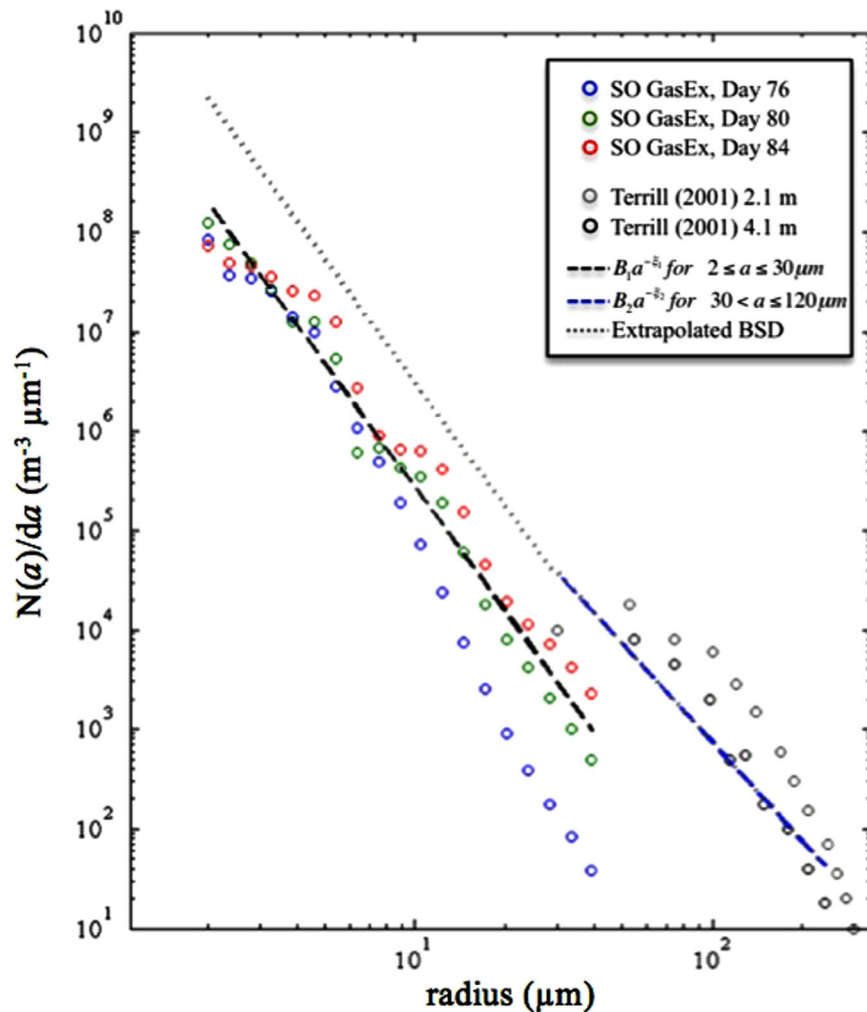

Figure 12. A single mean BSD (black dashed line), calculated from the mean BSDs measured on yeardays 76 (blue circles), 80 (green circles), and 84 (red circles) at 6–9 m in the Southern Ocean, was extrapolated to a depth of 4.1 m using a power law fit to the SO GasEx and *Terrill et al.* [2001] BSDs (gray circles) following equation (8) for $2 \leq a \leq 30$ (gray dotted line) and $30 < a \leq 120$ (blue dashed line). The power law fit to the SO GasEx and *Terrill et al.* [2001] data yielded N values of 3.39×10^9 and 2.44×10^9 and ξ values of 4.1 and 3.3, respectively. Bubbles $30 < a \leq 120$ μm in size contributed 6.3×10^{-7} (64%) of the total void fraction of 9.8×10^{-7}, while the smallest bubbles, $2 \leq a \leq 30$ μm, contributed 3.5×10^{-7} (36%).
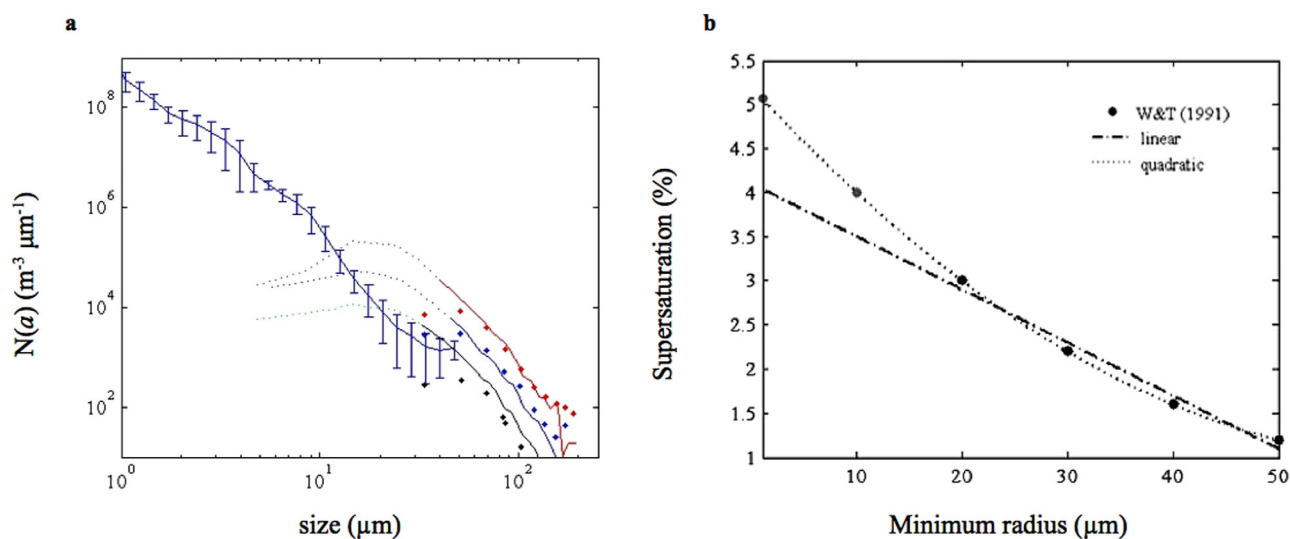
Figure 13. (a) *Moore et al*. [2011] estimated the bubble-mediated contribution to O_2 supersaturation to be 1%– 2% at 5 m during yeardays 76 and 84, respectively, using (a) the data of *Johnson and Cooke* [1979] at 0.7 m (red line), 1.8 m (blue line), and 4 m (black line) and (b) the model of *Woolf and Thorpe* [1991].For a 13 m s^{-1} wind speed, the model suggests that a maximum of 3% supersaturation will result using Johnson and Cooke's data, for which the minimum bubble radius is 20 μm (Figure 13b, black dots). Using the average bubble size distribution (BSD) measured during SO GasEx with a minimum radius of 1 μm (Figure 13a, blue line, with standard deviation), the predicted oxygen equilibrium supersaturation at 14 m s^{-1} wind speeds (gray dots) assuming a quadratic relationship (dotted line) and a linear relationship (dot-dashed line) suggest maximum suspersaturations of up to 4 and 5%, respectively.

relationship the wind and wavefield dynamics. However, these are some of the first measurements of such small bubbles at depth, particularly under natural wave breaking conditions, and their evolution, persistence, and potential contribution to air-sea flux of lower solubility gases is considered further below.

4.1. Measurements of Small Bubbles at Depth

The bubble size distributions presented here were collected during 13 m s^{-1} mean wind speeds. Though the mean wind speed was consistent throughout the three stations, the prevailing sea state produced bubble clouds with different intensities and therefore, different size distributions. The state of the wavefield is a function of the energy flux from the wind (i.e., wind history and fetch) [*Thorpe*, 1992; *Sullivan and McWilliams*, 2010]. The wind history (along an increasing trend) likely contributed to the nature of the bubble size distributions measured on yearday 76. During day 76, younger seas and shallower bubble penetration depths were measured. As a result, steeper bubble size distribution slopes and fewer large bubbles were measured (see Figure 7). Large breaking events under strong forcing led to the vertical extension of bubble plumes deep into the surface water column on yeardays 80 and 84. Bubble penetration depths of up to 15 m, more than $3H_s$, were measured. During days 80 and 84, bubble measurements were collected within a decreasing wind trend (from 15 m s^{-1}). Larger bubble sizes and shallower bubble size distribution slopes were measured at these stations.

The *Thorpe* [1992] parameterization relating bubble plume penetration depth to the wavelength of the dominant waves produced normalized penetration depths of 0.1–0.2 under forcing conditions comparable to those in the presented here. The Thorpe approach, modified here using the characteristic wavelength, produced a near 1:1 relationship between the mean bubble plume penetration depth and mean characteristic wavelength. For SO GasEx, the penetration depth scaling according to significant wave height follows $H_s < d_o < 4H_s$.

The average Southern Ocean bubble size distributions show a general consistency with previously measured bubble size distributions. The order of magnitude difference in concentration between those measured here and the previously published bubble distributions is likely due to the depth of measurement; here, bubble size distributions were collected near the base of the bubble plumes. This is particularly true for yearday 76, during which steep slopes were measured at the base of the bubble plumes. On yeardays 84 and 80, bubble measurements were collected approximately three quarters of the way down the plume,

due to the deep vertical extension of bubbles. As a result, bubble size distributions measured on those days produced slopes comparable to previously published values.

The Southern Ocean bubble size distributions measured as a part of this study decreased exponentially from small to large sizes and were not peaked. Many previously published bubble size distributions measurements show a hypothetical peak in the distribution between 20 and 60 μm that tails off at smaller sizes [i.e., *Johnson and Cooke*, 1979; *Kolovayev*, 1976; *Walsh and Mulhearn*, 1987] (see Figure 8). The presence of the peak has been justified theoretically due to the pressure effects on bubbles at depth. The peak at intermediate sizes, and the narrowing of the bubble size distribution with depth, has been attributed to the smallest bubbles having undergone dissolution and large, buoyant bubbles rising out of the water column. However, the presence of a peak could be the result of limitations in the acoustic and photographic methods used [*Kingsbury and Marston*, 1981; *Vagle and Farmer*, 1992]. A new optical approach applied by *Zhang et al.* [2002] for retrieving the bubble size distribution using inversion techniques supported the existence of submicron bubbles with concentrations on the order of 10^{12} m^{-3}. These results provide additional support for the presence of bubbles down to submicron sizes with concentrations following a power law distribution.

Detection of small bubbles at 6–9 m supports the existence of a mechanism that prolongs the process of bubble dissolution, aiding in their temporary persistence. The stabilization of microbubbles by the adsorption of organic substances could be at play here. Organic coatings can make bubbles mechanically stable by hindering compression and altering buoyancy, thus increasing residence times. Once coated, microbubbles have a size-dependent resistance to pressure, where resistance is inversely proportional to size [*Johnson and Cooke*, 1980]. Laboratory experiments by *Thorpe et al.* [1992] tested the effects of incrementally increasing particulate concentrations on bubble size distributions at 4 m depth. The result was a steep bubble size distribution (no peak) covering a range in radii from 0 to 10 μm, as was observed in the SO GasEx bubble size distributions. In the absence of candidate coating material, *Thorpe et al.* [1992] observed a peak in the bubble size distribution at $a \approx 40$ μm, where small bubbles fell off steeply due to rapid dissolution. The *Thorpe et al.* [1992] results in combination with the particulate and total and dissolved organic carbon measured during SO GasEx support the hypothesis that the bubbles measured here are coated [*Detwiler and Blanchard*, 1978; *Thorpe et al.*, 1992].

4.2. Evolution and Persistence of Small Bubbles

Deep-going bubble plumes evolve mainly under the influence of advection, turbulent diffusion, dissolution, and buoyancy forces [*Thorpe*, 1982; *Baldy*, 1988]. Bubbles in the size regime measured here (<60 um) are thought to completely disappear by dissolution [*Merlivat and Memery*, 1983; *Keeling*, 1993]. Small bubbles measured during SO GasEx were measured over time periods on the order of 10–100 s. The potential fate of the bubbles measured here was investigated by analyzing changes in the size distribution over time. We expected that the SO GasEx bubble size distributions would maintain a flatter size distribution slope throughout bubble events, since the principle loss mechanism was likely dissolution. No statistically significant trends were observed in the bubble size distribution slope over time for the older seas encountered on yeardays 80 and 84. We hypothesize that the small bubbles were terminated by dissolution at a rate independent of size, which would result in a constant slope [*Garrett et al.*, 2000]. For the younger seas encountered on yearday 76 and measurements made closer to the base of the bubble plume, a slight steepening in slope was observed over time, indicating the potential for preferential loss of larger bubbles. This result could indicate buoyancy as the dominant bubble removal process [*Garrett et al.*, 2000].

4.3. Small Bubble Contribution to the Void Fraction

If dissolution is the dominant mechanism by which the deeply penetrating SO GasEx bubbles are terminated, then they could be relevant to the transfer and supersaturation of the surface ocean with low-solubility gases in near-equilibrium conditions [*Woolf and Thorpe*, 1991; *Garrett et al.*, 2000]. Void fractions for the bubble densities measured at 6–9 m depth ranged from 10^{-7} to 10^{-9} and were composed entirely of bubbles from 0.5 to 60 μm in size. The volume contribution of air by the smallest size classes ($a < 10$ μm), previously unmeasured, was not negligible. As small bubbles are incrementally included in the integration from large to small sizes, the total void fraction continues to increase, though at a lower rate relative to that contributed by larger ($a > 10$ μm) bubble sizes (Figure 9). Exclusion of the smallest bubbles in the calculation of the total void fraction would ultimately result in an underestimation by over an order of magnitude.

Void fractions of this magnitude are considered to be insignificant when compared to the void fractions of 10^{-2} to 10^{-4} found near the surface. It is the deep-going bubbles, however, that contribute to the supersaturation of lower-solubility gases. The supersaturating effect of bubbles increases linearly with depth [*Woolf and Thorpe*, 1991; *Woolf*, 1997]. In order to assess the contribution of small bubbles to the void fraction at shallower depths, the mean SO GasEx bubble size distribution was extrapolated to 4 m using the data of *Terrill et al.* [2002], extending the SO GasEx bubble size distribution to 125 μm. The SO GasEx bubble size distribution at 4 m produced a total void fraction O(10^{-6}). Bubbles 30–125 μm in size contributed 64% of the void fraction. The remaining 36% of the void fraction was supplied by bubbles less than 30 μm in radius.

Dissolved O_2 was generally near saturation or supersaturated during SO GasEx, specifically throughout yeardays 76 and 84 discussed here (no O_2 data were collected during yearday 80) [*Moore et al.*, 2011]. According to *Moore et al.* [2011], diffusive and bubble-mediated processes, rather than vertical entrainment (i.e., mixing), were largely responsible for the exchange and supersaturation of low-solubility gases during SO GasEx. The analysis of *Moore et al.* [2011] estimates the bubble contribution to O_2 using the peaked bubble size distribution of Johnson and Cooke, extending only to 30 μm. The supersaturating effect of bubbles during high wind conditions (i.e., 13 m s^{-1}) could exceed the estimated 1–2% and account for a larger portion of the measured supersaturation (perhaps up to 4–5%) by extending the bubble size distribution down to 1 μm.

5. Conclusions

Measurements of critical angle ($\sim$80°) scattering, which only arise from the difference in refractive index between air and water, and near-forward scattering together can be used to detect very small bubbles. Here measurements of scattered light at the critical angle with the MASCOT instrument and near-forward scattering with the LISST instrument demonstrated the presence of small bubbles at 6–9 m depth in the Southern Ocean. These are some of the first measurements of deeply penetrating bubbles under natural wave-breaking conditions and in different sea states.

Near-forward scattering of red light measured with the LISST instrument was used to estimate the bubble size distribution down to a bubble radius of 0.5 μm. Here, exponentially increasing concentrations of bubbles were found down to the smallest size class. This is one of the first studies to use the LISST to directly measure bubbles and we have noted several potential errors associated with the instrument. However, there was strong agreement between the bubble number concentration and size distribution slope between those measured here and from previously published research for the commonly measured size classes.

Bubbles measured during SO GasEx were exclusively very small bubbles ($a < 60$ μm) producing void fractions O($10^{-8}-10^{-7}$). Extrapolation of the bubble size distributions measured at 6–9 to 4 m depth extended the maximum bubble size to 120 μm radius and produced a void fraction on the order of 10^{-6}. Although mainly composed of the larger bubbles, the small (<30 μm radius) previously neglected bubbles supplied 36% of the total void fraction. Therefore, the nature of the bubble size distribution down to the smallest size classes is particularly relevant in quantifying the bubble-mediated transfer and supersaturation of low-solubility gases. The supersaturating effect of bubbles could exceed the estimated 1–2%–4–5% by extending the bubble size distribution down to 1 μm.

The data set presented here is limited to only a handful of stations; nonetheless, it provides a foundation for more theoretical and experimental research on the existence, prevalence, persistence, and implications of such small bubbles in the ocean. Future research will involve further validation of and investigation into the presence and fate of such small bubbles, including their size distributions, the associated physical mechanisms producing the plumes, and their contribution to air-sea gas flux.

References

Agrawal, Y. C., and H. C. Pottsmith (2000), Instruments for particle size and settling velocity observations in sediment transport, *Mar. Geol.*, *168*(1–4), 89–114, doi:10.1016/S0025-3227(00)00044-X.

Agrawal, Y. C., and P. Traykovski (2001), Particles in the bottom boundary layer: Concentration and size dynamics through events, *J. Geophys. Res.*, *106*(C5), 9533–9542, doi:10.1029/2000JC900160.

Andrews, S. W., D. M. Nover, J. E. Reuter, and S. G. Schladow (2011), Limitations of laser diffraction for measuring fine particles in oligotrophic systems: Pitfalls and potential solutions, *Water Resour. Res.*, *47*, W05523, doi:10.1029/2010WR009837.

Babanin, A. V., M. L. Banner, I. R. Young, and M. A. Donelan (2007), Wave-follower field measurements of the wind-input spectral function. Part III: Parameterization of the wind-input enhancement due to wave breaking, *J. Phys. Oceanogr.*, *37*(11), 2764–2775, doi:10.1175/2007JPO3757.1.

Balch, W. M., D. T. Drapeau, B. C. Bowler, E. Lyczskowski, E. S. Booth, and D. Alley (2011), The contribution of coccolithophores to the optical and inorganic carbon budgets during the Southern Ocean Gas Exchange Experiment: New evidence in support of the ''Great Calcite Belt'' hypothesis, *J. Geophys. Res.*, *116*, C00F06, doi:10.1029/2011JC006941.

Baldy, S. (1988), Bubbles in the close vicinity of breaking waves: Statistical characteristics of the generation and dispersion mechanism, *J. Geophys. Res.*, *93*(C7), 8239–8248, doi:10.1029/JC093iC07p08239.

Banner, M. L., and R. P. Morison (2010), Refined source terms in wind wave models with explicit wave breaking prediction. Part I: Model framework and validation against field data, *Ocean Modell.*, *33*(1–2), 177–189, doi:10.1016/j.ocemod.2010.01.002.

Breitz, N. D., and H. Medwin (1989), Instrumentation for in situ acoustical measurements of bubble spectra under breaking waves, *J. Acoust. Soc. Am.*, *86*, 739–743.

Broecker, H. C., and W. Siems (1984), The role of bubbles for gas transfer from water to air at higher windspeeds: Experiments in the wind-wave facility in Hamburg, in *Gas Transfer at Water Surfaces*, edited by W. Brutsaert and G. H. Jirka, pp. 229–236, Kluwer Acad., Dordrecht, Holland.

Brooks, I. M., et al. (2009), Physical exchanges at the air–sea interface: UK–SOLAS field measurements, *Bull. Am. Meteorol. Soc.*, *90*(5), 629–644, doi:10.1175/2008BAMS2578.1.

Buonassissi, C. J., and H. M. Dierssen (2010), A regional comparison of particle size distributions and the power law approximation in oceanic and estuarine surface waters, *J. Geophys. Res.*, *115*, C10028, doi:10.1029/2010JC006256.

Cifuentes-Lorenzen, A., J. B. Edson, C. J. Zappa, and L. Bariteau (2013), A multisensor comparison of ocean wave frequency spectra from a research vessel during the southern ocean gas exchange experiment, *J. Atmos. Oceanic Technol.*, *30*, 2907–2925, doi:10.1175/JTECH-D-12–00181.1.

Cifuentes-Lorenzen, A. P. (2013), The wave boundary layer over the open ocean and the implications to air-sea interaction, PhD dissertation, Univ. of Conn., Storrs.

Czerski, H., M. Twardowski, X. Zhang, and S. Vagle (2011), Resolving size distributions of bubbles with radii less than 30 μm with optical and acoustical methods, *J. Geophys. Res.*, *116*, C00H11, doi:10.1029/2011JC007177.

Deane, G. B., and M. D. Stokes (2002), Scale dependence of bubble creation mechanisms in breaking waves, *Nature*, *418*(6900), 839–844, doi:10.1038/nature00967.

Detwiler, A., and D. C. Blanchard (1978), Aging and bursting bubbles in trace-contaminated water, *Chem. Eng. Sci.*, *33*(1), 9–13, doi:10.1016/0009–2509(78)85061-1.

Edson, J. B., C. W. Fairall, L. Bariteau, C. J. Zappa, A. Cifuentes-Lorenzen, W. R. McGillis, S. Pezoa, J. E. Hare, and D. Helmig (2011), Direct covariance measurement of CO_2 gas transfer velocity during the 2008 Southern Ocean Gas Exchange Experiment: Wind speed dependency, *J. Geophys. Res.*, *116*, C00F10, doi:10.1029/2011JC007022.

Farmer, D. M., and S. Vagle (1989), Waveguide propagation of ambient sound in the ocean-surface bubble layer, *J. Acoust. Soc. Am.*, *86*(5), 1897–1908.

Farmer, D. M., S. Vagle, and A. D. Booth (1998), A free-flooding acoustical resonator for measurement of bubble size distributions, *J. Atmos. Oceanic Technol.*, *15*(5), 1132–1146, doi:10.1175/1520-0426(1998)015<1132:AFFARF>2.0.CO;2.

Fournier, G. R., and J. L. Forand (1994), Analytic phase function for ocean water, in *Ocean Optics XII* [online], vol. *2258*, edited by J. S. Jaffe, pp. 194–201, SPIE, The International Society for Optics and Photonics, Bergen, Norway. [Available at http://dx.doi.org/10.1117/12.190063.]

Garrett, C., M. Li, and D. Farmer (2000), The connection between bubble size spectra and energy dissipation rates in the upper ocean, *J. Phys. Oceanogr.*, *30*(9), 2163–2171, doi:10.1175/1520-0485(2000)030<2163:TCBBSS>2.0.CO;2.

Gemmrich, J. R., M. L. Banner, and C. Garrett (2008), Spectrally resolved energy dissipation rate and momentum flux of breaking waves, *J. Phys. Oceanogr.*, *30*, 2163–2171.

Hamme, R. C., and S. R. Emerson (2006), Constraining bubble dynamics and mixing with dissolved gases: Implications for productivity measurements by oxygen mass balance [online], *J. Mar. Res.*, *64*(1), 73–95. [Available at http://www.escholarship.org/uc/item/6c08x8p3.].

Ho, D. T., C. L. Sabine, D. Hebert, D. S. Ullman, R. Wanninkhof, R. C. Hamme, P. G. Strutton, B. Hales, J. B. Edson, and B. R. Hargreaves (2011), Southern ocean gas exchange experiment: Setting the stage, *J. Geophys. Res.*, *116*, C00F08, doi:10.1029/2010JC006852.

Johnson, B. D., and R. C. Cooke (1979), Bubble populations and spectra in coastal waters: A photographic approach, *J. Geophys. Res.*, *84*(C7), 3761–3766, doi:10.1029/JC084iC07p03761.

Johnson, B. D., and R. C. Cooke (1980), Organic particle and aggregate formation resulting from the dissolution of bubbles in seawater, *Limnol. Oceanogr.*, *25*(4), 653–661.

Keeling, R. F. (1993), On the role of large bubbles in air-sea gas exchange and supersaturation in the ocean, *J. Mar. Res.*, *51*(2), 237–271, doi:10.1357/0022240933223800.

Kingsbury, D. L., and P. L. Marston (1981), Mie scattering near the critical angle of bubbles in water, *J. Opt. Soc. Am.*, *71*(3), 358–361.

Kolovayev, P. A. (1976), Investigation of the concentration and statistical size distribution of wind-produced bubbles in the near-surface ocean layer, Oceanology, *Engl. Transl.*, *15*, 659–661.

Medwin, H. (1970), In situ acoustic measurements of bubble populations in coastal ocean waters, *J. Geophys. Res.*, *75*(3), 599–611, doi:10.1029/JC075i003p00599.

Medwin, H. (1977), In situ acoustic measurements of microbubbles at sea, *J. Geophys. Res.*, *82*(6), 971–976, doi:10.1029/JC082i006p00971.

Medwin, H., and N. D. Breitz (1989), Ambient and transient bubble spectral densities in quiescent seas and under spilling breakers, *J. Geophys. Res.*, *94*(C9), 12,751–12,759, doi:10.1029/JC094iC09p12751.

Merlivat, L., and L. Memery (1983), Gas exchange across an air-water interface: Experimental results and modeling of bubble contribution to transfer, *J. Geophys. Res.*, *88*(C1), 707–724, doi:10.1029/JC088iC01p00707.

Mobley, C. D., L. K. Sundman, and E. Boss (2002), Phase function effects on oceanic light fields, *Appl. Opt.*, *41*(6), 1035–1050.

Monahan, E. C., and M. C. Spillane (1984), The role of oceanic whitecaps in air sea gas exchange, in *Gas Transfer at Water Surfaces*, edited by W. Brutsaert and G. H. Jirka, pp. 495–504, D. Reidel, Norwell, Mass.

Moore, T. S., M. D. DeGrandpre, C. L. Sabine, R. C. Hamme, C. J. Zappa, W. R. McGillis, R. A. Feely, and W. M. Drennan (2011), Sea surface pCO_2 and O_2 in the Southern Ocean during the austral fall, 2008, *J. Geophys. Res.*, *116*, C00F11, doi:10.1029/2010JC006560.

O'Hern, T. J., L. D'Agostino, and A. J. Acosta (1988), Comparison of holographic and coulter counter measurement of cavitation nuclei in the ocean, *J. Fluids Eng.*, *110*, 200–207.

Pascal, R. W., et al. (2010), A spar buoy for high-frequency wave measurements and detection of wave breaking in the open ocean, *J. Atmos. Oceanic Technol.*, *28*(4), 590–605, doi:10.1175/2010JTECHO764.1.

Phelps, A. D., and T. G. Leighton (1998), Oceanic bubble population measurements using a buoy-deployed combination frequency technique, *IEEE J. Oceanic Eng.*, *23*(4), 400–410, doi:10.1109/48.725234.

Su, M. Y., S. C. Ling, and J. Cartmill (1987), Optical microbubble measurements in the North Sea, in *Proceedings of Workshop on Natural Mechanisms of Surface Generated Noise*, NATO ASI Ser., Ser. C, Kluwer Acad, Lerici, Italy.

Sullivan, J. M., and M. S. Twardowski (2009), Angular shape of the oceanic particulate volume scattering function in the backward direction, *Appl. Opt.*, *48*(35), 6811–6819.

Sullivan, P., and J. McWilliams (2010), Dynamics of winds and currents coupled to surface waves, *Ann. Rev. Fluid Mech.*, *42*(1), 19–42, doi: 10.1146/annurev-fluid-121108–145541.

Terray, E., M. Donelan, Y. Agrawal, W. Drennan, K. Kahma, A. Williams, P. Hwang, and S. Kitaigorodskii (1996), Estimates of kinetic energy dissipation under breaking waves, *J. Phys. Oceanogr.*, *26*, 792–807.

Terrill, E. J., W. K. Melville, and D. Stramski (2001), Bubble entrainment by breaking waves and their influence on optical scattering in the upper ocean, *J. Geophys. Res.*, *106*(C8), 16,815–16,823, doi:10.1029/2000JC000496.

Thorpe, S. (1986), Measurements with an automatically recording inverted echo sounder; ARIES and the bubble clouds, *J. Phys. Oceanogr.*, *16*(8), 1462–1478.

Thorpe, S., P. Bowyer, and D. Woolf (1992), Some factors affecting the size distributions of oceanic bubbles, *J. Phys. Oceanogr.*, *22*, 382–389.

Thorpe, S. A. (1982), On the clouds of bubbles formed by breaking wind-waves in deep water, and their role in air-sea gas transfer, *Philos. Tran. R. Soc. London, Ser. A*, *304*(1483), 155–210.

Thorpe, S. A. (1992), Bubble clouds and the dynamics of the upper ocean, *Q. J. R. Meteorol. Soc.*, *118*, 1–22.

Twardowski, M., X. Zhang, S. Vagle, J. Sullivan, S. Freeman, H. Czerski, Y. You, L. Bi, and G. Kattawar (2012), The optical volume scattering function in a surf zone inverted to derive sediment and bubble particle subpopulations, *J. Geophys. Res.*, *117*, C00H17, doi:10.1029/2011JC007347.

Twardowski, M. S., E. Boss, J. M. Sullivan, and P. L. Donaghay (2004), Modeling the spectral shape of absorption by chromophoric dissolved organic matter, *Mar. Chem.*, *89*(1–4), 69–88, doi:10.1016/j.marchem.2004.02.008.

Vagle, S., and D. M. Farmer (1992), The measurement of bubble-size distributions by acoustical backscatter, *J. Atmos. Oceanic Technol.*, *9*(5), 630–644, doi:10.1175/1520-0426(1992)009<0630:TMOBSD>2.0.CO;2.

Vagle, S., and D. M. Farmer (1998), A comparison of four methods for bubble size and void fraction measurements, *IEEE J. Oceanic Eng.*, *23*(3), 211–222, doi:10.1109/48.701193.

Vagle, S., C. McNeil, and N. Steiner (2010), Upper ocean bubble measurements from the NE Pacific and estimates of their role in air-sea gas transfer of the weakly soluble gases nitrogen and oxygen, *J. Geophys. Res.*, *115*, C12054, doi:10.1029/2009JC005990.

Walsh, A. L., and P. J. Mulhearn (1987), Photographic measurements of bubble populations from breaking wind waves at sea, *J. Geophys. Res.*, *92*(C13), 14,553–14,565, doi:10.1029/JC092iC13p14553.

Woolf, D. K. (1997), Bubbles and their role in air-sea gas exchange, in *The Sea Surface and Global Change*, edited by P. S. Liss and R. A. Duce, pp. 173–205, Cambridge Univ. Press, New York.

Woolf, D. K., and S. A. Thorpe (1991), Bubbles and the air-sea exchange of gases in near-saturation conditions, *J. Mar. Res.*, *49*(3), 435–466, doi:10.1357/002224091784995765.

Woolf, D. K., et al. (2007), Modelling of bubble-mediated gas transfer: Fundamental principles and a laboratory test, *J. Mar. Syst.*, *66*(1–4), 71–91, doi:10.1016/j.jmarsys.2006.02.011.

Zhang, X., M. Lewis, M. Lee, B. Johnson, and G. Korotaev (2002), The volume scattering function of natural bubble populations, *Limnol. Oceanogr.*, *47*(5), 1273–1282.

Zhang, X., M. Twardowski, and M. Lewis (2011), Retrieving composition and sizes of oceanic particle subpopulations from the volume scattering function, *Appl. Opt.*, *50*(9), 1240–1259.